







# Constraining the redshift of PG 1553+113 using the photohadronic model

Sarira Sahu<sup>1</sup> , R. de J. Pacheco-Aké<sup>2</sup> , G. Sánchez-Colón<sup>2</sup> , D. I. Páez-Sánchez<sup>1</sup> ,  
A. U. Puga Oliveros<sup>1</sup>  Subhash Rajpoot<sup>3</sup> ,

<sup>1</sup>*Instituto de Ciencias Nucleares, Universidad Nacional Autónoma de México, Circuito Exterior S/N, C.U., A.P. 70-543, CDMX 04510, México.*

<sup>2</sup>*Departamento de Física Aplicada, Centro de Investigación y de Estudios Avanzados del IPN, Unidad Mérida. A.P. 73, Cordemex, Mérida, Yucatán 97310, México.*

<sup>3</sup>*Department of Physics and Astronomy, California State University, 1250 Bellflower Boulevard, Long Beach, CA 90840, USA.*

## ABSTRACT

Between 2005 and 2015, the BL Lacertae object PG 1553+113 exhibited multiple very high-energy (VHE;  $> 100$  GeV) gamma-ray flares, which were detected by the Cherenkov telescopes, High Energy Stereoscopic System (HESS), Major Atmospheric Gamma Imaging Cherenkov (MAGIC), and the Very Energetic Radiation Imaging Telescope Array System (VERITAS). Despite the uncertainty surrounding its redshift ( $z$ ), various studies have sought to estimate this value. In this study, seventeen independently observed VHE gamma-ray spectra of PG 1553+113 are analyzed using four distinct extragalactic background light (EBL) models alongside the photohadronic framework. A global  $\chi^2$  fit is applied to all observational data to determine the best-fitting redshift for each EBL model. Additionally, confidence level (CL) intervals for the redshift are calculated across all EBL models. The findings demonstrate that the photohadronic framework effectively describes all observed spectra. Among the EBL models, the lowest total  $\chi^2$  value of 58.82 (with 58 degrees of freedom) was obtained using the model from [Saldana-Lopez et al. \(2021\)](#), while the highest value of 75.67 was associated with the model from [Dominguez et al. \(2011\)](#). The 95 per cent CL intervals for the statistical error of the redshift of PG 1553+113 are  $0.500 < z < 0.537$  for the [Saldana-Lopez et al. \(2021\)](#) model and  $0.491 < z < 0.527$  for the [Dominguez et al. \(2011\)](#) model. These results highlight the consistency of the photohadronic approach in interpreting the observed VHE gamma-ray spectra.

**Key words:** BL Lacertae objects: individual: PG 1553+113, galaxies: distances and redshifts, methods: statistical

## 1 INTRODUCTION

BL Lacertae (BL Lac) blazars represent a unique category of active galactic nuclei (AGN), distinguished by their non-thermal emission spectra, which arise from a relativistic jet oriented nearly parallel to the observer’s line of sight ([Urry & Padovani 1995](#); [Acciari et al. 2011](#)). These objects display rapid variability across the entire electromagnetic spectrum. Their spectral energy distributions (SEDs) are marked by a characteristic two-peak structure ([Abdo et al. 2010b](#)). The low-energy peak is attributed to the synchrotron radiation emitted by the low-energy electrons as they traverse the jet’s magnetic field. The high-energy peak, on the other hand, can be either due to the inverse Compton scattering of high-energy electrons with their self-produced synchrotron pho-

tons—referred to as synchrotron self-Compton (SSC) scattering ([Maraschi et al. 1992](#); [Dermer & Schlickeiser 1993](#); [Sikora et al. 1994](#); [Blazewski et al. 2000](#); [Murase et al. 2012](#); [Gao et al. 2013](#))—or the scattering of external photons originating from the accretion disk, broad-line regions, or the dusty torus surrounding the AGN ([Dermer & Schlickeiser 1993](#); [Sikora et al. 1994](#); [Blazewski et al. 2000](#)).

In BL Lac objects, the non-thermal radiation significantly overshadows the stellar light emitted by their host galaxies, making it challenging to determine accurately the redshifts. This limitation creates uncertainties in studying the cosmic evolution, deciphering the source’s characteristics, and analyzing its intrinsic VHE spectrum. Given that VHE photons are absorbed by the EBL, obtaining precise redshift measurements is essential for understanding the EBL’s influence on VHE photons.

PG 1553+113, a well-known blazar, was first identified in a photographic survey ([Green et al. 1986](#)). Its spectral properties have been thoroughly examined, leading to its classification as a high-frequency synchrotron peaked BL Lac (HBL) ([Chang et al. 2019](#)). Over the years, multiple VHE

\* Contact e-mail: [sarira@nucleares.unam.mx](mailto:sarira@nucleares.unam.mx)

† Contact e-mail: [rodrigo.pacheco@cinvestav.mx](mailto:rodrigo.pacheco@cinvestav.mx)

‡ Contact e-mail: [gabriel.sanchez@cinvestav.mx](mailto:gabriel.sanchez@cinvestav.mx)

§ Contact e-mail: [diana.paez@correo.nucleares.unam.mx](mailto:diana.paez@correo.nucleares.unam.mx)

¶ Contact e-mail: [angel.puga@correo.nucleares.unam.mx](mailto:angel.puga@correo.nucleares.unam.mx)

|| Contact e-mail: [Subhash.Rajpoot@csulb.edu](mailto:Subhash.Rajpoot@csulb.edu)

observations have been carried out using different instruments. The HESS telescope array first detected this blazar in gamma-rays in 2005 (Aharonian et al. 2006), and it was later monitored by MAGIC and VERITAS in various campaigns between 2005 and 2015, especially during periods of heightened activity.

The VHE gamma-ray flux from a blazar ( $F_\gamma$ ), as measured on Earth, can be expressed as (Hauser & Dwek 2001):

$$F_\gamma(E_\gamma) = F_{\text{int}}(E_\gamma) e^{-\tau_{\gamma\gamma}(E_\gamma, z)}, \quad (1)$$

where  $E_\gamma$  denotes the energy of the observed VHE photon,  $F_\gamma$  is the observed flux, and  $F_{\text{int}}$  represents the intrinsic flux. The optical depth,  $\tau_{\gamma\gamma}$ , which arises from the pair production process  $\gamma\gamma \rightarrow e^+e^-$ , is a function of both  $E_\gamma$  and the redshift  $z$  of the source. The exponential term in Eq. (1) signifies the reduction in VHE flux caused by  $e^+e^-$  pair production (Stecker et al. 1992; Ackermann et al. 2012; Padovani et al. 2017). As a result, determining the redshift with precision is critical for deriving the intrinsic flux from the observed measurements. To analyze VHE gamma-ray spectra from sources at different redshifts, the Imaging Atmospheric Cherenkov Telescopes (IACTs) collaborations rely on well-established EBL models developed by Franceschini et al. (2008); Finke et al. (2010); Dominguez et al. (2011); Gilmore et al. (2012); Saldana-Lopez et al. (2021).

The redshift of PG 1553+113 has not been directly measured but has been inferred through various methods. Using data from HESS observations in 2005 and considering the absorption of VHE gamma-rays by the EBL, Aharonian et al. (2006) derived an upper limit of  $z < 0.74$ . Later, Danforth et al. (2010) established a lower limit of  $0.4 < z$  by detecting intervening Ly  $\alpha$  absorbers, while also setting an upper limit of  $z < 0.58$  due to the absence of Ly  $\beta$  absorbers at  $z > 0.4$ . Subsequent studies have supported these constraints. For instance, Aliu et al. (2015) analyzed the time-averaged VHE spectrum from VERITAS observations between 2010 and 2012, incorporating EBL evolution, and proposed a redshift upper limit of  $z \leq 0.62$ . More recently, Dorigo Jones et al. (2022) used a Ly  $\alpha$ -forest-based approach to suggest a narrower redshift range of  $0.408 < z < 0.436$ . Our study aims to estimate the redshift of PG 1553+113 using the photohadronic model, employing a statistical approach and a comprehensive dataset.

The photohadronic model (Sahu 2019) has previously been applied successfully to interpret the VHE gamma-ray spectra of HBLs and extreme HBLs (EHBLs) (Sahu et al. 2020, 2021, 2022). In this work, the photohadronic model (Sahu 2019) is combined with four established EBL models (Franceschini et al. (2008); Dominguez et al. (2011); Gilmore et al. (2012); Saldana-Lopez et al. (2021)) to analyze seventeen VHE flaring events of PG 1553+113 observed between 2005 and 2015 by the HESS, VERITAS, and MAGIC collaborations. By performing a global  $\chi^2$  fit to the experimental data from these VHE spectra, central values and CL intervals for the redshift of PG 1553+113 are determined for each EBL model. This method has been validated in prior analyses, such as the redshift constraint determination for the BL Lac object PKS 1424+240, which aligned with spectroscopic measurements (Sahu et al. 2024).

The structure of this paper is organized as follows. Section 2 provides an overview of the seventeen independent observations of PG 1553+113 used in the analysis. Section 3

offers a concise review of the photohadronic model and its relevance to this study. Section 4 presents the analysis and results, while Section 5 concludes with a summary and discussion of the findings.

## 2 VHE OBSERVATIONS OF PG 1553+113

This section provides a concise overview of the seventeen observations of PG 1553+113 by different Cherenkov telescopes which we analyze here to constrain the redshift. Key details for each observation are summarized in Table 1. To simplify referencing, each observation is labeled according to the telescope and the year it was conducted. For instance, the HESS observation of 2005 is labeled as H05.

### 2.1 H05, H06

In reference Aharonian et al. (2008), a re-analysis of the 2005 HESS data (7.6 hours) for PG 1553+113 (Aharonian et al. 2006) is presented, incorporating an improved calibration of the detector's absolute energy scale. Additionally, results from 17.2 hours of HESS observations conducted in 2006 are reported.

HESS conducted VHE observations of PG 1553+113 in 2005 and 2006. Near-infrared spectroscopy in the  $H+K$  band ( $1.45\text{--}2.45\ \mu\text{m}$ ) was performed in March 2006 using the Spectrograph for INtegral Field Observations in the Near Infrared (SINFONI), an integral field spectrometer on the European Southern Observatory (ESO) Very Large Telescope (VLT) in Chile.

Over the two years of observations (totaling 24.8 hours of live time), HESS detected a VHE signal with a significance of approximately 10 standard deviations. No significant flux or spectral variations were observed on any time scale within the VHE data. Despite the high sensitivity of the SINFONI spectrum, which is among the most detailed near-infrared spectra ever obtained for this object, no absorption or emission lines were identified, preventing a determination of the redshift.

A total of 30.3 hours of HESS observations were conducted, typically in segments of about 28 minutes (runs), during 2005 and 2006. The telescopes were offset by  $\pm 0.5^\circ$  from the position of PG 1553+113 during these observations. After applying data-quality selection criteria, the useful exposure time amounted to 24.8 hours of live time, with 9 of the 66 runs excluded. The 2005 observation, referred to as H05, had a live time of 7.6 hours, while the 2006 observation, labeled H06, had a live time of 17.2 hours.

### 2.2 H12

The HESS telescopes observed significant flaring activity in the VHE gamma-ray emissions from the HBL PG 1553+113. Notably, the source's flux enhanced by a factor of about three on the nights of April 26 and 27, 2012, compared to previous archival measurements, with indications of variability within the same night. Interestingly, during this period *Fermi* Large Area Telescope did not detect any signal. Using Bayesian statistical approach to the above data, the redshift was found to be  $z = 0.49 \pm 0.04$  (Abramowski et al. 2015).

As discussed previously, the observations H05 and H06 showed no signs of variability and are collectively termed

as the “pre-flare” data set. This pre-flare data set comprises 26.4 hours of high-quality live time observations. During the 2012 flaring period (referred here as H12), eight observational runs, each lasting approximately 28 minutes were conducted on April 26 and 27, totaling 3.5 hours of live time. All observations were performed in wobble mode, where the source is positioned at an offset of  $0.5^\circ$  from the centre of the instrument’s field of view. This method resulted in acceptance-corrected live times of 24.8 hours for the pre-flare data and 3.2 hours for the flare data.

### 2.3 H13

The HESS phase II, with a fifth telescope CT5, observed the HBL PG 1553+113 in 2013 between May 29 and August 9, 2013 (MJD 56441–56513) (H.E.S.S. Collab. et al. 2017), referred to as H13 in this work. These observations are divided into 28-minute segments called runs and conducted in wobble mode, where the camera’s field of view is offset by  $0.5^\circ$  or  $0.7^\circ$  from the source position, either along the right-ascension or declination axis. For this analysis, only runs with the source positioned between  $0.35^\circ$  and  $1.2^\circ$  from the camera centre were included. During the commissioning phase, some runs employed non-standard wobble offsets to evaluate the instrument’s performance. This approach ensures the source remains well within the field of view and facilitates accurate background subtraction.

### 2.4 M0506

The MAGIC telescope detected VHE gamma-ray emissions from the HBL PG 1553+113 during observations conducted in 2005 and 2006. The signal achieved an overall significance of 8.8 standard deviations over a total observation time of 18.8 hours. The spectrum did not exhibit significant daily flux variations and the flux levels in 2005 were notably higher than those recorded in 2006. The combined differential energy spectrum for PG 1553+113 from these two years is presented in reference Albert et al. (2007) and is referred to as M0506 in this work. Observations of PG 1553+113 with the MAGIC telescope took place in two main periods: 8.9 hours in April and May 2005, coinciding with HESS observations (Aharonian et al. 2008), and 19 hours from January to April 2006.

To ensure data quality, observations affected by poor weather conditions or hardware issues were excluded from the analysis. Additionally, only data collected at small zenith angles ( $< 30^\circ$ ), which correspond to a lower energy threshold suitable for studying steep energy spectra, were included. Although measurements extended up to zenith angles of  $53^\circ$ , the final analysis retained 7.0 hours of high-quality data from 2005 and 11.8 hours from 2006 after applying these selection criteria.

### 2.5 M06

The MAGIC telescope observed PG 1553+113 during a multiwavelength campaign from July 14 to July 27, 2006, accumulating 9.5 hours of data at zenith angles ranging between  $18^\circ$  and  $35^\circ$  (Albert et al. 2009). These observations are labeled as M06 in this study. The data were collected in wobble mode, with the source positioned at an offset of  $\pm 0.4^\circ$  from

the camera’s centre, allowing simultaneous measurement of both the source and the background. Approximately one hour of data was discarded due to technical issues.

The quality of the data set was impacted by calima, a phenomenon involving Saharan sand-dust in the atmosphere, which caused nightly atmospheric absorption levels to vary between 5 and 40 per cent. To address the attenuation of Cherenkov light, correction factors were computed and applied to the affected data. After these adjustments, a signal with a significance of 5.0 standard deviations was detected in 8.5 hours of observation.

### 2.6 M07, M08, M09

Following its initial detection, PG 1553+113 became a regular target for observations with the MAGIC telescope. As reported in reference Aleksić et al. (2012), new data collected in 2007, 2008, and 2009 were analyzed, and here we refer to these observations as M07, M08, and M09, respectively. Since the autumn of 2009, MAGIC has operated as a stereo system consisting of two IACTs located on La Palma in the Canary Islands, Spain. However, the data discussed here were acquired before this upgrade, using only the single MAGIC I telescope.

As mentioned previously, PG 1553+113 was observed by MAGIC for approximately 19 hours in 2005 and 2006 (Albert et al. 2007) and was also the focus of a multiwavelength campaign in July 2006 involving optical, X-ray, and TeV gamma-ray (Albert et al. 2009). Reference Aleksić et al. (2012) presents the results of follow-up observations conducted for 14 hours in March–April 2007, nearly 26 hours in March–May 2008 (some of which were simultaneous with observations by other instruments (Aleksić et al. 2010)), and about 24 hours in March–July 2009, with some of the latter taken under moderate moonlight conditions. Unfortunately, the 2008 and 2009 observations were significantly impacted by adverse weather, including calima (Saharan sand dust in the atmosphere), which reduced the usable data and increased the energy threshold.

Rigorous quality cuts based on event rates after night sky background suppression were applied to the data. After these cuts, 28.7 hours of high-quality data remained, comprising 11.5 hours from 2007, 8.7 hours from 2008, and 8.5 hours from 2009. Combining the results from these three years, the 28.7 hours of observations yielded a signal with an overall significance of 8.8 standard deviations. The individual significances were 5.8 standard deviations for 2007, 8.1 for 2008, and 4.2 for 2009.

### 2.7 M08II

A comprehensive simultaneous multi-frequency observational campaign was conducted between March and April 2008, involving data collection across optical, X-ray, high-energy (HE) gamma-ray, and VHE gamma-ray bands (Aleksić et al. 2010). The average VHE differential spectrum of PG 1553+113 derived from these observations is reported and labeled as M08II in this work.

The MAGIC observations for this campaign took place on March 16–18 and April 13, 28–30, 2008, with zenith angles ranging from 18 to 36 degrees. Observations were conducted

in wobble mode, where the source was positioned at a 0.4-degree offset from the camera centre, alternating directions every 20 minutes. After applying standard quality cuts and filtering based on trigger rates, a total of 7.18 hours of effective observation time was retained for analysis.

To reconstruct the gamma-ray spectrum, looser selection criteria were employed to ensure that over 90 per cent of simulated gamma photons were preserved. The impact of varying cut efficiencies, ranging from 50 to 95 per cent across the energy spectrum, was examined to assess systematic effects on the spectral shape. Corrections were applied to data affected by calima.

Analysis of the MAGIC data revealed an excess of 415 gamma-like events compared to 1835 normalized background events, resulting in a detection significance of 8.0 standard deviations.

## 2.8 M12

In early 2012, PG 1553+113 entered a high state, and by April of that year, it reached its highest recorded VHE flux level to date. A comprehensive multiwavelength observation campaign was conducted from February to June 2012, aimed at characterizing the SED and studying the variability of the source across different frequency bands with observations spanned from VHE gamma-rays to radio wavelengths.

Reference [Aleksić et al. \(2015\)](#) details the analysis of flux variability in the VHE, HE, and X-ray bands. MAGIC observed PG 1553+113 from February 26 (MJD 55983) to April 26 (MJD 56043), 2012. After applying quality cuts, the data set comprised 18.3 hours of observations with zenith angles ranging from 17 to 34 degrees. Observations were conducted in wobble mode, with the source positioned 0.4 degrees from the camera centre. The standard MAGIC analysis chain was used to process the data, yielding an energy threshold of approximately 70 GeV. The source was detected with a high statistical significance ( $> 70$  standard deviations) during the February–April 2012 period, with the emission consistent with a point-like source at the location of PG 1553+113. Based on the flux levels, the data were divided into two subsets: MJD 55983–MJD 56016 (high state) and MJD 56037–MJD 56043 (flare state). During the flare, the VHE flux nearly doubled compared to the high state. The analysis of the VHE spectrum focuses on the April flare state, which is referred to as M12 in this work.

## 2.9 M12II, M12III, M13, M14, M15

In reference [Acciari et al. \(2019\)](#), a total of 32 MAGIC spectra were utilized to derive constraints on the EBL through a joint likelihood analysis of 12 blazars observed during extensive campaigns, amounting to over 300 hours of exposure. All data included in this study were collected during dark nights under optimal weather conditions.

Among these, five data sets correspond to the BL Lac object PG 1553+113, covering observations from 2012 to 2015 with a combined observation time of 66.36 hours. These data sets, as reported in reference [Acciari et al. \(2019\)](#), are labeled as PG1553+113.0202 (referred to here as M12II), PG1553+113.0203 (M12III), PG1553+113.0302 (M13), PG1553+113.0303 (M14), and PG1553+113.0306 (M15).

## 2.10 V1012

The time-averaged VERITAS spectrum for the BL Lac object PG 1553+113, covering observations from 2010 to 2012 (referred to in this work as V1012), is analyzed in reference [Aliu et al. \(2015\)](#).

VERITAS, an IACTs array, can detect PG 1553+113 at energies above 100 GeV with a significance of 5 standard deviations in approximately 43 minutes of observation, based on its average flux.

Observations of PG 1553+113 were conducted by VERITAS from May 2010 to June 2012, totaling 95 hours of observation time. Data were collected in wobble mode, with the source positioned at a 0.5-degree offset from the telescope's pointing direction to enable simultaneous background estimation. The zenith angles for these observations ranged from 20 to 30 degrees, with an average of 23 degrees. The combination of low zenith angles and event selection cuts optimized for soft-spectrum sources resulted in an analysis energy threshold (the energy at which the photon rate peaks after cuts) of 180 GeV.

The analysis used a circular signal region centered on the source's nominal position, extending radially outward by 0.14 degrees. After applying quality selection criteria based on weather conditions and instrument stability, and accounting for instrument read-out dead time, a total of 80 hours of live time were retained. These observations yielded an overall detection significance of 53 standard deviations, with the excess consistent with a point-like source at the location of PG 1553+113.

## 3 THE PHOTOHADRONIC MODEL

The photohadronic model proposes a double jet configuration during the VHE flaring process ([Sahu 2019; Sahu et al. 2019](#)). This configuration, previously suggested in earlier studies ([Ghisellini & Tavecchio 2008; Giannios et al. 2010](#)), involves a narrower, more compact jet of size  $R'_f$  embedded within a broader jet of size  $R'_b$ , where  $R'_f < R'_b$  (quantities in the comoving frame are denoted by primes). The photon density in the inner jet region,  $n'_{\gamma,f}$ , is significantly higher than in the outer region,  $n'_\gamma$  ( $n'_{\gamma,f} \gg n'_\gamma$ ). The model builds on the conventional interpretation of the first two peaks in the SED: the first peak arises from synchrotron radiation emitted by relativistic electrons in the jet, while the second peak results from the inverse Compton scattering process.

The inner jet is assumed to move at a slightly higher velocity, characterized by a bulk Lorentz factor  $\Gamma_{\text{in}}$ , compared to the outer jet with  $\Gamma_{\text{ext}}$ . For simplicity, it is assumed that  $\Gamma_{\text{in}} \simeq \Gamma_{\text{ext}} \equiv \Gamma$ , and both share a common Doppler factor  $\mathcal{D}$  ([Ghisellini et al. 1998; Krawczynski et al. 2004](#)). In the case of HBLs,  $\Gamma \simeq \mathcal{D}$ .

In this scenario, protons are accelerated to extremely high energies within the inner jet region, following a power-law energy distribution,  $dN_p/dE_p \propto E_p^{-\alpha}$  ([Dermer & Schlickeiser 1993](#)), where  $E_p$  is the proton energy and  $\alpha \geq 2$  is the proton spectral index. The value of  $\alpha$  varies depending on the type of shock involved, such as non-relativistic, highly relativistic, or oblique relativistic shocks ([Keshet & Waxman 2005; Summerlin & Baring 2012](#)). These high-energy protons interact with SSC background photons in the inner jet, producing  $\Delta$ -resonances via the process  $p + \gamma \rightarrow \Delta^+$ . The  $\Delta$ -resonance

decays into neutral and charged pions with different probabilities. While direct single-pion and multi-pion production processes also contribute, they are less efficient in the energy range considered here (Mücke et al. 1999; Owen et al. 2018), and their contributions are neglected in this work. The neutral pions decay into gamma-rays ( $\pi^0 \rightarrow \gamma\gamma$ ), while the charged pions decay into neutrinos ( $\pi^+ \rightarrow e^+ \nu_e \nu_\mu \bar{\nu}_\mu$ ) (Sahu et al. 2012). In the photohadronic model, the gamma-rays from  $\pi^0$  decay are blue-shifted to VHE energies and detected on Earth, while the positrons from  $\pi^+$  decay emit synchrotron radiation.

The observed VHE gamma-ray energy  $E_\gamma$  and the seed photon energy  $\epsilon_\gamma$  are related by the condition (Sahu 2019; Sahu et al. 2019)

$$E_\gamma \epsilon_\gamma \simeq 0.032 \frac{D^2}{(1+z)^2} \text{ GeV}^2. \quad (2)$$

In this process, the VHE photon carries roughly 10 per cent of the proton energy, such that  $E_p = 10E_\gamma$ . Due to the inaccessibility of the inner jet region and the absence of direct methods to measure the photon density within it, a scaling relationship is assumed between the photon densities in the inner and outer jet regions. This relationship can be expressed as (Sahu et al. 2016)

$$\frac{n'_{\gamma,f}(\epsilon_{\gamma,1})}{n'_{\gamma,f}(\epsilon_{\gamma,2})} \simeq \frac{n'_\gamma(\epsilon_{\gamma,1})}{n'_\gamma(\epsilon_{\gamma,2})}, \quad (3)$$

where the left-hand side represents the unknown photon density ratio in the inner jet region, and the right-hand side corresponds to the known ratio in the outer jet region. This equation allows the unknown photon density in the inner region to be expressed in terms of the measurable photon density in the outer region.

The intrinsic gamma-ray flux resulting from the decay of  $\pi^0$  particles is derived as

$$F_{\text{int}}(E_\gamma) \equiv E_\gamma^2 \frac{dN(E_\gamma)}{dE_\gamma} \propto E_p^2 \frac{dN(E_p)}{dE_p} n'_{\gamma,f}. \quad (4)$$

By incorporating the seed photon density and the proton flux, the intrinsic flux can be expressed in the form

$$F_{\text{int}}(E_\gamma) = F_0 \left( \frac{E_\gamma}{\text{TeV}} \right)^{-\delta+3}, \quad (5)$$

where  $F_0$  is a normalization factor. Substituting this into Eq. (1), the observed flux is given by

$$F_\gamma(E_\gamma) = F_0 \left( \frac{E_\gamma}{\text{TeV}} \right)^{-\delta+3} e^{-\tau_{\gamma\gamma}(E_\gamma, z)}, \quad (6)$$

where  $\tau_{\gamma\gamma}(E_\gamma, z)$  accounts for the absorption of gamma-rays due to interactions with the EBL. The spectral index  $\delta$  is defined as  $\delta = \alpha + \beta$ , where  $\alpha$  is the proton spectral index and  $\beta$  represents the power-law behavior of the seed photon spectrum in the low-energy tail of the SSC spectrum. The normalization factor  $F_0$  is determined from observational data, while  $\delta$  serves as the sole free parameter in the photohadronic model (Sahu et al. 2019). As evident from Eq. (6), any curvature in the spectrum can be attributed to the exponential absorption term (Acciari et al. 2019).

It is worth emphasizing that the photohadronic process is most effective for gamma-ray energies  $E_\gamma \gtrsim 100$  GeV. At lower energies, leptonic processes such as electron synchrotron radiation and the SSC mechanism dominate the multiwavelength SED.

## 4 ANALYSIS AND RESULTS

We analyze all the seventeen observations discussed in Sec. 2 in the context of the photohadronic model to constrain the redshift of the HBL PG 1553+113. To account for the EBL correction to the VHE gamma-ray spectra, we use four well known and widely used EBL models. Here, these models are referred to as Saldana (Saldana-Lopez et al. 2021), Franceschini (Franceschini et al. 2008), Domínguez (Domínguez et al. 2011), and Gilmore (Gilmore et al. 2012).

Following the classification scheme proposed by Sahu et al. (2019), the VHE emission states of a HBL are defined based on the value of the spectral index  $\delta$ . A very high emission state corresponds to  $2.5 \leq \delta \leq 2.6$ , a high emission state to  $2.6 < \delta < 3.0$ , and a low emission state to  $\delta = 3.0$ . Since PG 1553+113 is a HBL,  $\delta$  is constrained to the range  $2.5 \leq \delta \leq 3.0$ . Given that the duration of observations varies across datasets, each observation is expected to represent a distinct emission state, necessitating independent values of  $\delta$ . Therefore,  $\delta$  is treated as a constrained but adjustable parameter during the fitting process.

To analyze the VHE spectra and determine the best fits, each EBL model is integrated into the photohadronic framework. A global  $\chi^2$  fit is performed on all data points by simultaneously varying the redshift  $z$  (common to all observations), the normalization constants  $F_0$ , and the spectral parameter  $\delta$  for each of the seventeen independent observations. This global fitting procedure is repeated for all four EBL models to identify the best-fitting values of  $z$ ,  $F_0$ , and  $\delta$ . Confidence level intervals for the statistical errors of the redshift at 68, 90, and 95 per cent of coverage probability are then calculated for each EBL model.

With 58 degrees of freedom (93 experimental data points and 35 free parameters), the minimum  $\chi^2$  values obtained for the global fit are 58.82, 65.50, 68.50, and 75.67 for the Saldana, Gilmore, Franceschini, and Domínguez EBL models, respectively. The best-fitting values for  $F_0$  and  $\delta$  for each observation, along with the corresponding EBL models, are shown in Table 2. Notably, the  $F_0$  values exhibit minor variations across EBL models for a given observation, indicating similarities among the models. The best-fitting redshift and its CL intervals at 68, 90, and 95 per cent are presented in Table 3. Each EBL model predicts slightly different CL intervals for  $z$ , reflecting variations in the models' predictions.

The fits to the seventeen observed VHE spectra of PG 1553+113 are illustrated in Fig. 1, using the best-fitting parameters from the Saldana EBL model (detailed in Tables 2 and 3). Fits based on the Domínguez, Franceschini, and Gilmore EBL models are not shown, as they are visually indistinguishable from those of the Saldana model.

For comparison, all four EBL models are applied to fit the spectrum of H13, as shown in Fig. 2. While all models provide excellent fits, a slight discrepancy is observed for  $E_\gamma \gtrsim 0.3$  TeV. Additionally, Table 4 summarizes the redshift constraints for PG 1553+113 estimated by various authors, including those derived in this work.

## 5 SUMMARY AND DISCUSSION

In this work, the photohadronic model is employed in conjunction with four EBL models—Saldana, Franceschini,

Domínguez, and Gilmore—to derive constraints on the redshift of the HBL PG 1553+113. The analysis incorporates seventeen independent VHE spectra collected by the HESS, MAGIC, and VERITAS telescopes between 2005 and 2015. The photohadronic model, which has been successfully applied in previous studies to constrain the redshifts of HBLs with unknown  $z$  values (Sahu 2019; Sahu et al. 2019), is used here to interpret the VHE spectra of PG 1553+113.

A global  $\chi^2$  fitting procedure is performed, simultaneously varying the redshift  $z$ , the normalization constants  $F_0$ , and the spectral parameter  $\delta$  for each of the seventeen observations, to identify the best fit to the observed VHE spectra for a given EBL model. This process is repeated for the remaining three EBL models to determine the optimal values of  $z$ ,  $F_0$ , and  $\delta$  for each case. Using these best-fitting parameters, CL intervals for the redshift at 68, 90, and 95 per cent are computed for each EBL model.

Notably, the 95 per cent CL intervals derived in this study show significant overlap with redshift estimates from previous works. In some cases, narrower intervals are achieved at high confidence levels, a result of the strong statistical support provided by the extensive dataset used in the fitting process. This underscores the robustness of the photohadronic model and the reliability of the EBL corrections applied in this analysis.

The photohadronic model, combined with EBL corrections, provides a reliable method for estimating the redshift of PG 1553+113. The results highlight the effectiveness of the photohadronic model in interpreting the VHE gamma-ray spectra and its potential application to other HBLs with unknown redshifts.

## ACKNOWLEDGEMENTS

R. de J. P-A and G. S-C thank SECIHTI (México) for its partial support. Partial support from CSU-Long Beach is gratefully acknowledged.

## DATA AVAILABILITY

No new data were generated or analyzed in support of this research.

## REFERENCES

- Abdo A. A., et al., 2010a, *ApJ*, **708**, 1310  
 Abdo A. A., et al., 2010b, *ApJ*, **716**, 30  
 Abramowski A., et al., 2015, *ApJ*, **802**, 65  
 Acciari V. A., et al., 2011, *ApJ*, **729**, 2  
 Acciari V. A., et al., 2019, *MNRAS*, **486**, 4233  
 Ackermann M., et al., 2012, *Science*, **338**, 1190  
 Aharonian F., et al., 2006, *A&A*, **448**, L19  
 Aharonian F., et al., 2008, *A&A*, **477**, 481  
 Albert J., et al., 2007, *ApJ*, **654**, L119  
 Albert J., et al., 2009, *A&A*, **493**, 467  
 Aleksić J., et al., 2010, *A&A*, **515**, A76  
 Aleksić J., et al., 2012, *ApJ*, **748**, 46  
 Aleksić J., et al., 2015, *MNRAS*, **450**, 4399  
 Aliu E., et al., 2015, *ApJ*, **799**, 7  
 Blazewski M., Sikora M., Moderski R., Madejski G., 2000, *ApJ*, **545**, 107  
 Chang Y. L., Arsioli B., Giommi P., Padovani P., Brandt C. H., 2019, *A&A*, **632**, A77  
 Danforth C. W., Keeney B. A., Stocke J. T., Shull J. M., Yao Y., 2010, *ApJ*, **720**, 976  
 Dermer C. D., Schlickeiser R., 1993, *ApJ*, **416**, 458  
 Domínguez A., et al., 2011, *MNRAS*, **410**, 2556  
 Dorigo Jones J., et al., 2022, *MNRAS*, **509**, 4330  
 Finke J. D., Razzaque S., Dermer C. D., 2010, *ApJ*, **712**, 238  
 Franceschini A., Rodighiero G., Vaccari M., 2008, *A&A*, **487**, 837  
 Gao H., Lei W.-H., Zhang B., 2013, *MNRAS*, **435**, 2520  
 Ghisellini G., Tavecchio F., 2008, *MNRAS*, **387**, 1669  
 Ghisellini G., Celotti A., Fossati G., Maraschi L., Comastri A., 1998, *MNRAS*, **301**, 451  
 Giannios D., Uzdensky D. A., Begelman M. C., 2010, *MNRAS*, **402**, 1649  
 Gilmore R. C., Somerville R. S., Primack J. R., Domínguez A., 2012, *MNRAS*, **422**, 3189  
 Green R. F., Schmidt M., Liebert J., 1986, *ApJS*, **61**, 305  
 H.E.S.S. Collab. et al., 2017, *A&A*, **600**, A89  
 Hauser M. G., Dwek E., 2001, *ARA&A*, **39**, 249  
 Keshet U., Waxman E., 2005, *PRL*, **94**, 111102  
 Krawczynski H., et al., 2004, *ApJ*, **601**, 151  
 Landoni, M. Falomo, R. Treves, A. Sbarufatti, B. 2014, *A&A*, **570**, A126  
 Malik Z., Sahayanathan S., Shah Z., Iqbal N., Manzoor A., Bhatt N., 2022, *MNRAS*, **511**, 994  
 Maraschi L., Ghisellini G., Celotti A., 1992, *ApJ*, **397**, L5  
 Mazin D., Goebel F., 2007, *ApJ*, **655**, L13  
 Mücke A., Rachen J. P., Engel R., Protheroe R. J., Stanev T., 1999, *PASA*, **16**, 160  
 Murase K., Dermer C. D., Takami H., Migliori G., 2012, *ApJ*, **749**, 63  
 Nicastro F., 2018, preprint ([arXiv:1811.03498](https://arxiv.org/abs/1811.03498))  
 Owen E. R., Jacobsen I. B., Wu K., Surajbali P., 2018, *MNRAS*, **481**, 666  
 Padovani P., et al., 2017, *A&AR*, **25**, 2  
 Prandini E., Dorner D., Mankuzhiyil N., Mariotti M., Mazin D., 2009, preprint ([arXiv:0907.0157](https://arxiv.org/abs/0907.0157))  
 Qin L., Wang J., Yan D., Yang C., Yuan Z., Zhou M., 2018, *MNRAS*, **473**, 3755  
 Sahu S., 2019, *Rev. Mex. Fis.*, **65**, 307  
 Sahu S., Zhang B., Fraija N., 2012, *Phys. Rev. D*, **85**, 043012  
 Sahu S., Miranda L. S., Rajpoot S., 2016, *EPJ. C*, **76**, 127  
 Sahu S., Fortín C. E. L., Nagataki S., 2019, *ApJ*, **884**, L17  
 Sahu S., López Fortín C. E., Castañeda Hernández L. H., Nagataki S., Rajpoot S., 2020, *ApJ*, **901**, 132  
 Sahu S., López Fortín C. E., Valadez Polanco I. A., Rajpoot S., 2021, *ApJ*, **914**, 120  
 Sahu S., Valadez Polanco I. A., Rajpoot S., 2022, *MNRAS*, **515**, 5235  
 Sahu S., Páez-Sánchez D. I., Medina-Carrillo B., Pacheco-Aké R. d. J., Sánchez-Colón G., Rajpoot S., 2024, *MNRAS*, **533**, 2156  
 Saldana-Lopez A., et al., 2021, *MNRAS*, **507**, 5144  
 Sikora M., Begelman M. C., Rees M. J., 1994, *ApJ*, **421**, 153  
 Stecker F. W., de Jager O. C., Salamon M. H., 1992, *ApJ*, **390**, L49  
 Summerlin E. J., Baring M. G., 2012, *ApJ*, **745**, 63

**Table 1.** Details of the seventeen PG 1553+113 observations used in this study are provided. The first and second columns list the observation name and the instrument used, respectively. The third, fourth, fifth, and sixth columns include the start date, end date, period span (in MJD), and live observation duration (in hours), respectively. The seventh column references the work where the data for each observation period is originally reported.

Observation	Instrument	Start date	End date	Period	Live duration	Reference
H05	HESS	2005 April	2005 August	53492-53614	7.6	Aharonian et al. (2008)
H06	HESS	2006 April	2006 July	53849-53943	17.2	Aharonian et al. (2008)
H12	HESS	2012 April 26	2012 April 27	56043-56044	3.2	Abramowski et al. (2015)
H13	HESS	2013 May 29	2013 August 9	56441-56513	16.8	H.E.S.S. Collab. et al. (2017)
M0506	MAGIC	2005 April	2006 April	–	18.8	Albert et al. (2007)
M06	MAGIC	2006 July 14	2006 July 27	53930-53943	8.5	Albert et al. (2009)
M07	MAGIC	2007 March 23	2007 April 24	54182-54214	11.5	Aleksić et al. (2012)
M08	MAGIC	2008 March 17	2008 May 7	54542-54593	8.7	Aleksić et al. (2012)
M08II	MAGIC	2008 March 16	2008 April 30	54541-54586	7.18	Aleksić et al. (2010)
M09	MAGIC	2009 April 16	2009 June 15	54937-54997	8.5	Aleksić et al. (2012)
M12	MAGIC	2012 April 20	2012 April 26	56037-56043	1.1	Aleksić et al. (2015)
M12II	MAGIC	2012 February 28	2012 March 4	55985-55990	2.4	Acciari et al. (2019)
M12III	MAGIC	2012 March 13	2012 May 2	55999-56049	24.84	Acciari et al. (2019)
M13	MAGIC	2013 April 7	2013 June 12	56389-56455	11.42	Acciari et al. (2019)
M14	MAGIC	2014 March 11	2014 March 25	56727-56741	1.93	Acciari et al. (2019)
M15	MAGIC	2015 January 25	2015 August 7	57047-57241	25.77	Acciari et al. (2019)
V1012	VERITAS	2010 May	2012 June	–	80	Aliu et al. (2015)

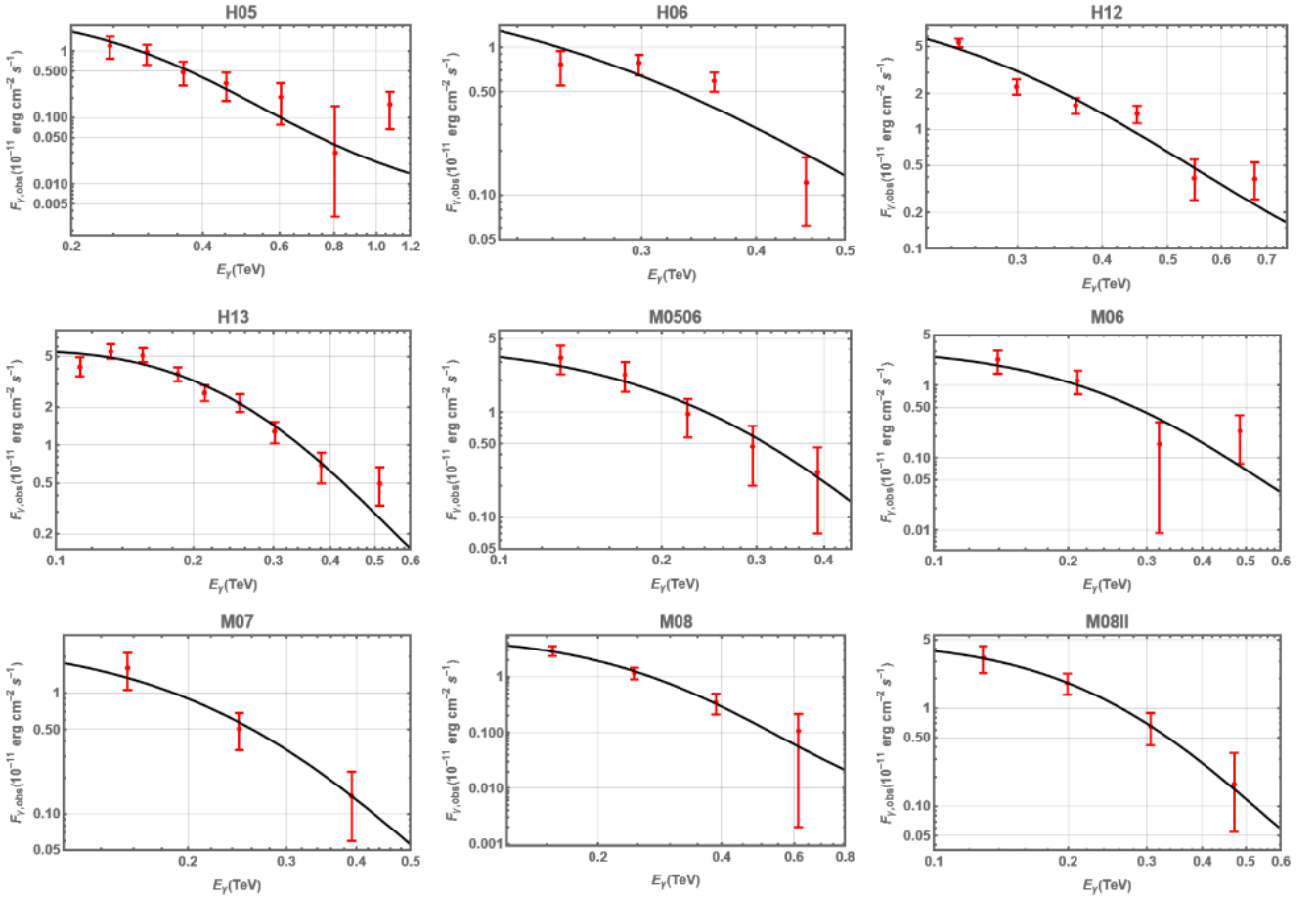


**Figure 1.** The photohadronic model, combined with the Saldana EBL model, is applied to fit the seventeen observed VHE gamma-ray spectra of PG 1553+113. The corresponding redshift is fixed at  $z = 0.518$ , while the normalization constants  $F_0$  and spectral parameters  $\delta$  are provided in Table 2.

**Table 2.** The best-fitting values for the normalization constant  $F_0$  (expressed in units of  $10^{-11} \text{ erg cm}^{-2} \text{ s}^{-1}$ ) and the spectral index  $\delta$  of the photohadronic model, determined from fitting the VHE spectra of PG 1553+113, are displayed in the third, fourth, seventh, and eighth columns. These results correspond to four distinct EBL models. The first and fifth columns identify the observations, while the second and sixth columns specify the EBL models applied, as outlined in the main text.

Observation	EBL Model	$F_0$	$\delta$	Observation	EBL Model	$F_0$	$\delta$
H05	Domínguez	11.14	2.50	H06	Domínguez	7.83	2.50
	Saldana	12.87	2.50		Saldana	9.05	2.50
	Franceschini	11.08	2.50		Franceschini	7.78	2.50
	Gilmore	12.15	2.50		Gilmore	8.54	2.50
H12	Domínguez	37.91	2.50	H13	Domínguez	14.29	2.66
	Saldana	43.41	2.50		Saldana	18.28	2.59
	Franceschini	37.60	2.50		Franceschini	14.71	2.63
	Gilmore	41.16	2.50		Gilmore	16.37	2.62
M0506	Domínguez	3.82	3.00	M06	Domínguez	2.82	3.00
	Saldana	4.39	3.00		Saldana	3.24	3.00
	Franceschini	3.78	3.00		Franceschini	2.80	3.00
	Gilmore	4.15	3.00		Gilmore	3.08	3.00
M07	Domínguez	2.27	3.00	M08	Domínguez	5.22	2.96
	Saldana	2.63	3.00		Saldana	6.23	2.93
	Franceschini	2.25	3.00		Franceschini	5.30	2.94
	Gilmore	2.48	3.00		Gilmore	5.78	2.95
M08II	Domínguez	4.80	2.97	M09	Domínguez	5.23	2.50
	Saldana	5.88	2.93		Saldana	6.03	2.50
	Franceschini	4.88	2.95		Franceschini	5.18	2.50
	Gilmore	5.39	2.95		Gilmore	5.70	2.50
M12	Domínguez	10.00	2.94	M12II	Domínguez	5.71	3.00
	Saldana	12.39	2.88		Saldana	6.41	3.00
	Franceschini	10.06	2.92		Franceschini	5.62	3.00
	Gilmore	11.21	2.91		Gilmore	6.14	3.00
M12III	Domínguez	8.77	2.88	M13	Domínguez	4.50	3.00
	Saldana	10.71	2.84		Saldana	5.27	2.97
	Franceschini	8.89	2.87		Franceschini	4.42	3.00
	Gilmore	9.83	2.86		Gilmore	4.82	3.00
M14	Domínguez	5.59	3.00	M15	Domínguez	4.70	3.00
	Saldana	6.19	3.00		Saldana	5.26	3.00
	Franceschini	5.49	3.00		Franceschini	4.62	3.00
	Gilmore	5.98	3.00		Gilmore	5.05	3.00
V1012	Domínguez	6.16	2.83				
	Saldana	6.99	2.84				
	Franceschini	6.20	2.82				
	Gilmore	6.72	2.83				

**Table 3.** The redshift values derived from the photohadronic model, based on a global  $\chi^2$  fit to the VHE spectra of PG 1553+113, are summarized. The first column identifies the EBL models used, as discussed in the main text. The second column provides the best-fitting redshift  $z$ , while the third, fourth, and fifth columns present the CL intervals for the statistical error at 68, 90, and 95 per cent, respectively, for each EBL model.

EBL Model	Redshift	Redshift CL intervals		
	$z$	68%	90%	95%
Domínguez	0.509	(0.500, 0.518)	(0.494, 0.524)	(0.491, 0.527)
Saldana	0.518	(0.509, 0.528)	(0.503, 0.534)	(0.500, 0.537)
Franceschini	0.515	(0.506, 0.524)	(0.500, 0.530)	(0.497, 0.533)
Gilmore	0.557	(0.547, 0.566)	(0.541, 0.573)	(0.538, 0.576)

Treves A., Falomo R., Uslenghi M., 2007, [A&A](#), 473, L17

Urry C. M., Padovani P., 1995, [PASP](#), 107, 803

Yang J., Wang J., 2010, [PASJ](#), 62, L23

This paper has been typeset from a  $\text{\LaTeX}$  file prepared by the author.

**Table 4.** A compilation of redshift estimates for PG 1553+113 from various studies is presented. The first column lists the redshift measurements, including interval limits or central values with associated uncertainties. The second column describes the methodologies employed to determine the redshift, while the third column cites the relevant references.

Redshift	Method	Reference
$0.491 < z < 0.527$ at 95 per cent CL	Global fit of the photohadronic model to independent observations (EBL Domínguez)	This work
$0.500 < z < 0.537$ at 95 per cent CL	Global fit of the photohadronic model to independent observations (EBL Saldana)	This work
$0.408 < z < 0.436$	Edge of the Ly $\alpha$ forest observed in UV spectra	<a href="#">Dorigo Jones et al. (2022)</a>
$z = 0.38 \pm 0.10$	VHE spectral index – redshift correlation	<a href="#">Malik et al. (2022)</a>
$z = 0.33 \pm 0.08$	VHE spectral index – redshift correlation	<a href="#">Malik et al. (2022)</a>
$0.22 < z < 0.48$	Leptonic model fit to multiple SEDs	<a href="#">Qin et al. (2018)</a>
$z = 0.3551$ and $z = 0.4339$	Analysis of OVII absorbers in the line of sight of the object	<a href="#">Nicastrò (2018)</a>
$z = 0.49 \pm 0.04$	Comparison of the hardness of different SEDs	<a href="#">Abramowski et al. (2015)</a>
$z \leq 0.62$	Energy spectrum and EBL evolution	<a href="#">Aliu et al. (2015)</a>
$0.3 < z$	X-Shooter spectroscopy	<a href="#">Landoni, M. et al. (2014)</a>
$z = 0.75^{+0.04}_{-0.05}$	Stepwise spectrum deabsorption and minimum $\chi^2$ fit	<a href="#">Abdo et al. (2010a)</a>
$0.43 < z \lesssim 0.58$	Detection (non-detection) of Ly $\alpha$ (Ly $\beta$ ) absorbers	<a href="#">Danforth et al. (2010)</a>
$z < 0.78$	Intrinsic and absorbed spectra comparison	<a href="#">Yang &amp; Wang (2010)</a>
$z < 0.67$	Constriction of the hardness of the spectrum	<a href="#">Prandini et al. (2009)</a>
$z < 0.69$	Parameter variation deabsorption	<a href="#">Aharonian et al. (2008)</a>
$z < 0.69$	Intrinsic photonic index limit	<a href="#">Mazin &amp; Goebel (2007)</a>
$0.3 < z < 0.4$	Constraint on the apparent magnitude of the host galaxy	<a href="#">Treves et al. (2007)</a>
$z < 0.74$	Parameter variation deabsorption	<a href="#">Albert et al. (2007)</a>
$z < 0.74$	Spectrum deabsorption	<a href="#">Aharonian et al. (2006)</a>

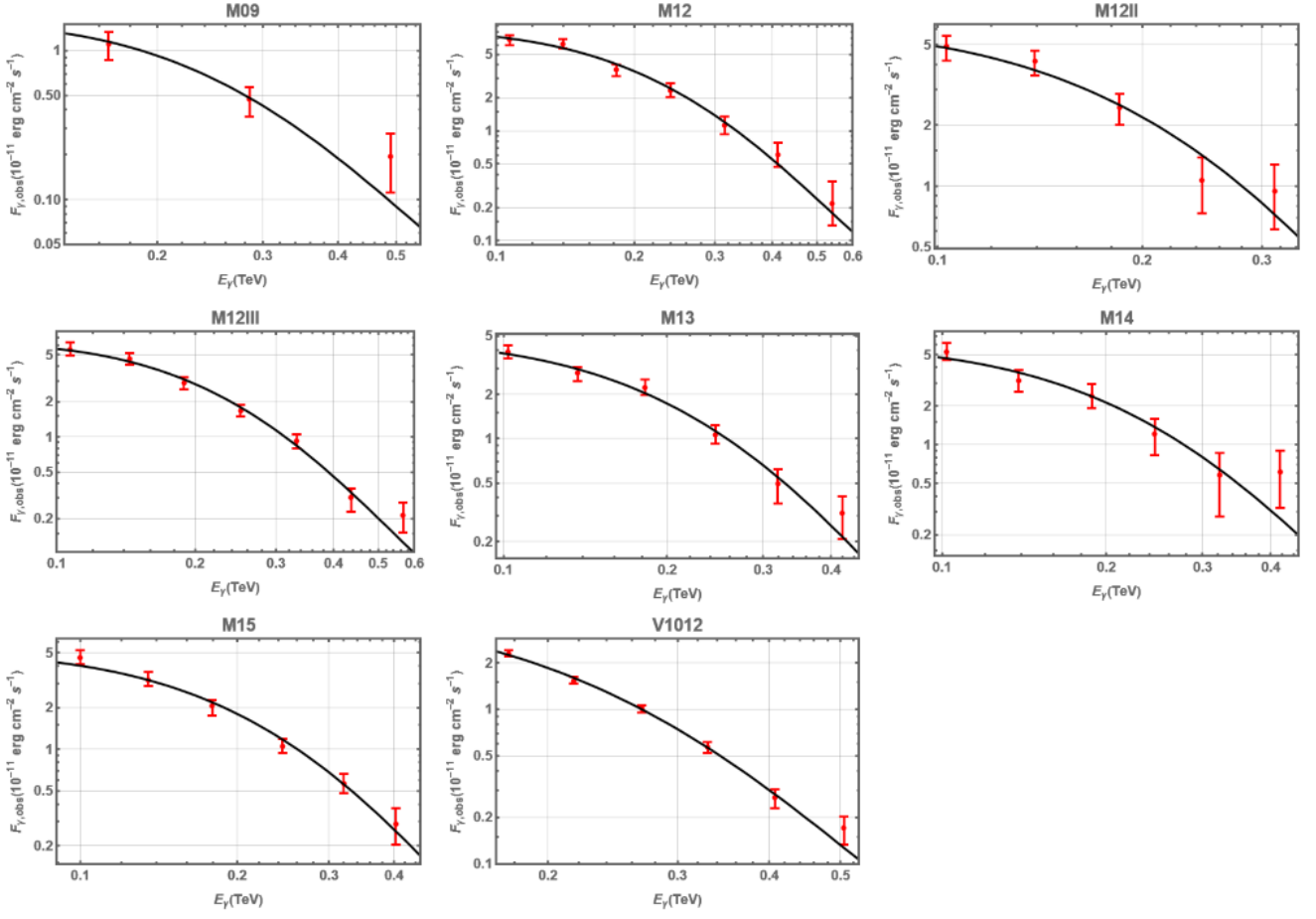


**Figure 1.** (Continued) The photohadronic model, combined with the Saldana EBL model, is applied to fit the seventeen observed VHE gamma-ray spectra of PG 1553+113. The corresponding redshift is fixed at  $z = 0.518$ , while the normalization constants  $F_0$  and spectral parameters  $\delta$  are provided in Table 2.

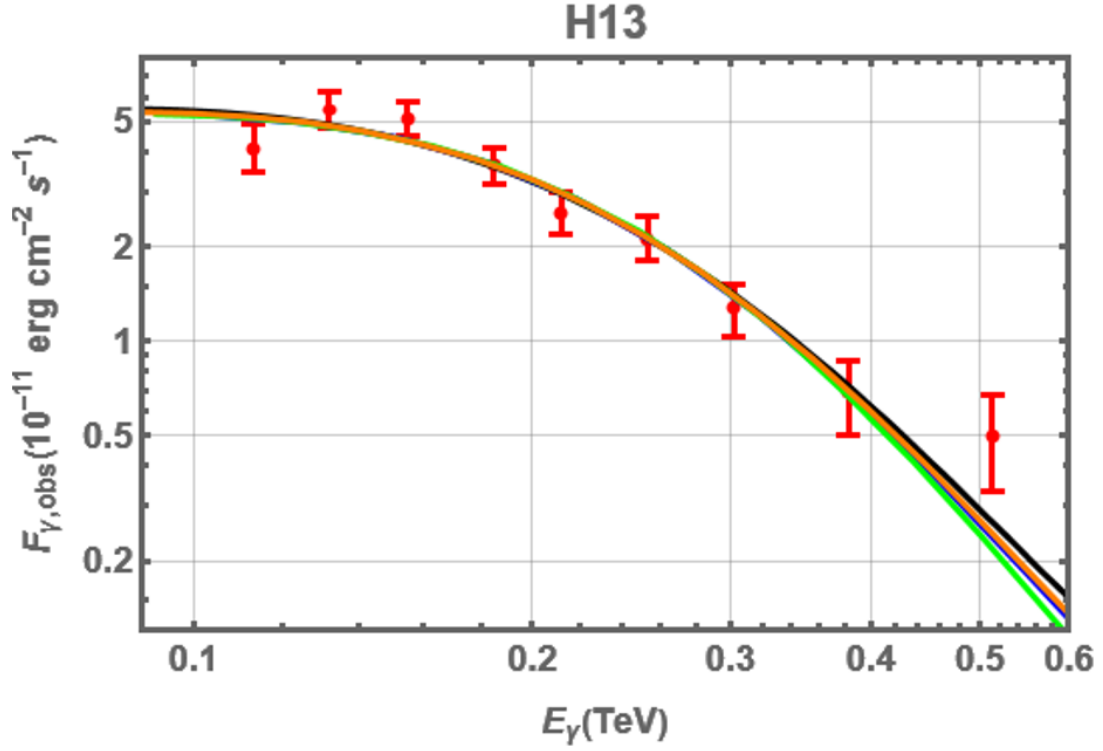


**Figure 2.** Fits of the photohadronic model to the observed VHE spectrum H13 of PG 1553+113 are presented to compare the performance of various EBL models: Saldana (black), Franceschini (blue), Domínguez (green), and Gilmore (orange). The associated values for the spectral parameter  $\delta$ , normalization constants  $F_0$ , and redshift  $z$  can be found in Tables 2 and 3.